Chemical Engineering Journal 425 (2021) 131678

Contents lists available at ScienceDirect

Chemical Engineering Journal

journal homepage: www.elsevier.com/locate/cej

Photocatalytic mineralization of indoor VOC mixtures over unique ternary $TiO_2/C/MnO_2$ with high adsorption selectivity

Wenjun Wang [a], Fawei Lin [a,*,1], Taicheng An [d], Saixi Qiu [e], Hongdi Yu [a], Beibei Yan [a], Guanyi Chen [b], Li-an Hou [c,*]

[a] *School of Environmental Science and Engineering, Tianjin University, Tianjin 300072, PR China*
[b] *School of Mechanical Engineering, Tianjin University of Commerce, Tianjin 300134, PR China*
[c] *Xi'an High-Tech Institute, Xi'an 710025, PR China*
[d] *Institute of Environmental Health and Pollution Control, School of Environmental Science and Engineering, Guangdong University of Technology, Guangzhou 510006, Guangdong, PR China*
[e] *College of Chemistry and Chemical Engineering, Qingdao University, Qingdao 266071, PR China*

ARTICLE INFO

Keywords:
Formaldehyde
Toluene
$TiO_2/C/MnO_2$ photocatalysts
Resource recovery
Indoor air purification

ABSTRACT

Formaldehyde (CH_2O) and toluene (C_7H_8) are typical indoor air pollutants that have high harm to people's health. Photocatalytic oxidation is a feasible approach, but still remains the problem of incomplete degradation to form refractory intermediates and uncertainty of interaction between multivariant components. This paper used natural proteins from waste shell as the carbon source and template to synthesize the ternary $TiO_2/C/MnO_2$ photocatalysts. It exhibited high adsorption selectivity and excellent photocatalytic performance for CH_2O and C_7H_8 mixture mineralization under visible light irradiation. The optimal candidate achieved near completely mineralization within 60 min in the simulated indoor environment and exhibited remarkable stability after 5 cycles. Large amounts of oxygen vacancies, lattice distortions of TiO_2, and tailored bandgap structure contributed to these excellent behaviors. Besides, carbon existence as an electron transfer channel dropped the interfacial charge-transfer resistance, thus prolonging the lifetime of charge carriers and making them rapidly go through the surface photo-oxidation reactions. In-situ DRIFTs results indicated that CH_2O and C_7H_8 mixtures possessed the same reaction pathway and rate-determining step with single component. Above all, this paper offered a facile, sustainable, and green approach to synthesize efficient photocatalysts for treating indoor CH_2O/C_7H_8 pollution with visible light irradiation.

1. Introduction

Indoor air quality is closely related to people's physical and mental health. The introduction of outdoor air pollutants and the release of indoor pollution sources will lead to serious indoor air pollution, which will endanger people's health. Up to now, photocatalytic technology is considered to have great potential for the degradation of volatile organic compounds (VOCs) and has been confirmed through its extensive application. Hou et al. synthesized an efficient N, Ca codoped TiO_2 photocatalyst by using the insoluble matrix proteins extracted from abalone shell for CH_2O degradation [1]. Dong and his groups combined thermocatalysis and photocatalysis into a serious MnO_2-based catalysts with high performance for indoor CH_2O elimination [2–4]. Zhang et al. successfully designed a direct ring-opening pathway for gas C_7H_8 removal, significantly improving the C_7H_8 purification performance [5]. However, most studies focused on the single-component system as part of air pollution. In fact, indoor air pollution is a complex issue with a multitude of VOCs existence concurrently. These components could react with each other to produce complex refractory intermediates, which also pose health hazards [6,7]. To resolve the problem, the photocatalysts are required to have high adsorption selectivity and strong photocatalytic oxidation to efficiently mineralize VOCs without producing potentially toxic and refractory intermediates.

In the current studies, TiO_2/MnO_2 has attracted much attention for its high catalytic oxidation. Huang et al. utilized O_3 which was generated under the vacuum ultraviolet radiation to increase the oxidation of

---

* Corresponding authors.
E-mail addresses: linfawei@tju.edu.cn (F. Lin), houla@cae.cn (L.-a. Hou).
[1] ORCID: https://orcid.org/0000-0001-5461-8277.

https://doi.org/10.1016/j.cej.2021.131678
Received 21 May 2021; Received in revised form 26 July 2021; Accepted 2 August 2021
Available online 10 August 2021

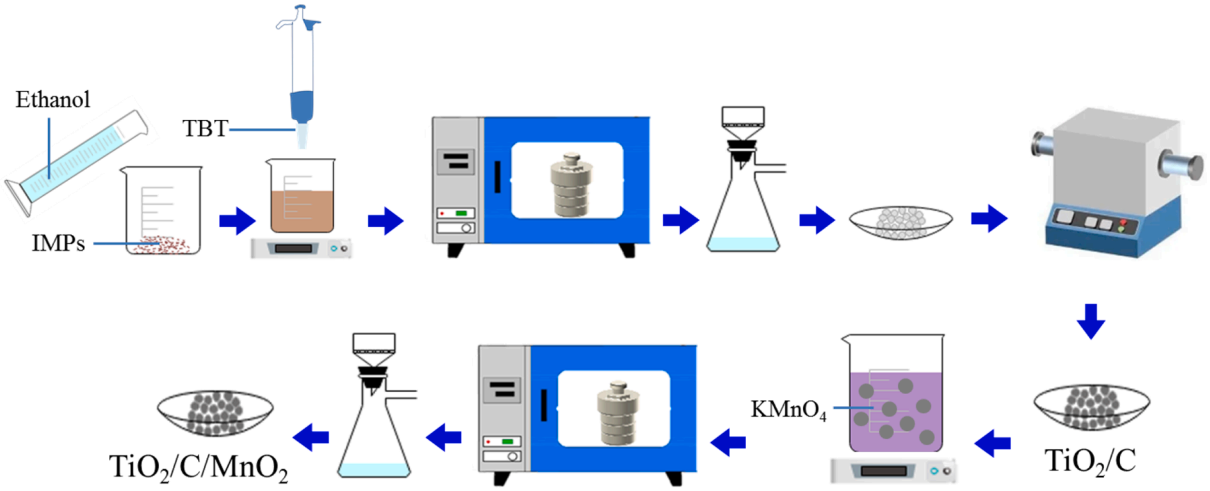

Scheme 1. Schematic diagram of catalysts preparation.

the system and improved the efficiency of toluene degradation [8]. Ji et al. applied MOx-TiFN in the photocatalytic ozonation of n-hexane [9]. Bergaoui et al. combined O_3 activation produced by non-thermal plasma and ultraviolet light (UV) technologies, enhancing the ethanol decomposition [10]. TiO_2/MnO_2 in coordination with O_3 oxidation is very efficient in industrial applications. However, this advancement is inapplicable to the indoor environment due to the latent health hazards of UV and O_3. As a consequence, the catalyst needs to be re-engineered to increase the separation efficiency between electrons and holes and promote electron transport for improving photocatalytic oxidation activity [11–13]. Carbon materials have these unique properties: low interfacial charge-transfer and photoelectronic coupling ability [14,15]. $TiO_2/C/MnO_2$ have already been synthesized and applied as supercapacitors, these studies clearly indicated that carbon enhances the interfacial relation between TiO_2 and MnO_2, as well as enhances electron transport throughout the composite materials [16–19]. Meanwhile, there are no reports about using $TiO_2/C/MnO_2$ for VOCs degradation, though it has big potential for this. The synthetic methods of previous work can be summarized as follows: Firstly, TiO_2 was used to deposit thin carbon layers. Secondly, MnO_2 substituted carbon layers. Finally, carbon layers were synthesized again to fabricate $TiO_2/C/MnO_2$. Nitrocellulose, glucose, starch and methanol et al. were usually used as the carbon source for carbon layers [15,18–20]. Complex steps or expensive materials can raise production costs and be hard to implement on a mass basis.

In our previous work, insoluble matrix proteins (IMPs) extracted from abalone shell waste were considered as a kind of effective template and dopant to synthesize TiO_2 and had the potential to be a good carbon source for $TiO_2/C/MnO_2$ [1]. In practical application, seashell waste which could be produced over 10 million tons since 2002 in China are used as Ca source for construction materials, calcium supplements or other materials [21]. IMPs in shell are discarded after recycling, inducing new environmental pollution [22]. These proteins can be broken into amino acids under solvothermal conditions [23–25]. These amino acids are rich in C and N elements and can serve as sacrificial bio-template, complexing agent and surfactant [26]. In this work, we synthesized $TiO_2/C/MnO_2$ with the assistance of IMPs as a carbon source and template for formaldehyde and toluene mixture (CH_2O and C_7H_8) degradation. This work was organized to conduct a comprehensive investigation consists of the following questions: (1) Whether IMPs can serve as a carbon source as natural materials to synthesize new construction $TiO_2/C/MnO_2$? (2) If so, whether it can act as an effective photocatalyst for mineralizing VOCs mixture? (3) What's the effect of coexistence between formaldehyde and toluene on the surface of $TiO_2/C/MnO_2$? (4) What's the photocatalytic degradation mechanism? These answers to these questions will be of great value in recycling seashell waste, indoor air purification and new sight on the VOC mixture degradation mechanism.

2. Experimental section

2.1. Catalyst preparation

IMPs preparation: The abalone shell washed by deionized water were demineralized in 5% acetic acid at ambient temperatures overnight to harvest IMPs. After separating and washing into pH neutral, IMPs were freeze-dried and sieved into 200-mesh.

Synthesis of TiO_2/C. The TiO_2/C were prepared by an IMPs-assisted solvothermal method. 0.4 g IMPs and 1.5 mL tetrabutyl titanate (TBT) were dispersed into a 30.0 mL anhydrous ethanol. Subsequently, the suspension was transferred to a 50.0 mL teflon-lined stainless-steel autoclave and heated at 200 °C for 50 h. After washing by anhydrous ethanol several times and drying at 80 °C, the obtained powder was carbonized at 500 °C under Ar atmosphere to harvest TiO_2/C. For comparison, the pristine TiO_2 was also prepared by the same method without IMPs.

Synthesis of $TiO_2/C/MnO_2$. After the carbonization process, MnO_2 was decorated in the TiO_2/C by in-situ redox reaction between carbon and $KMnO_4$. 0.75 g TiO_2/C was dispersed into a 30.0 mL $KMnO_4$ solution. Then, the mixture was placed into a 50.0 mL teflon-lined stainless-steel autoclave to maintain at 120 °C for 5 h. After washing with anhydrous ethanol and deionized water, the obtained powder was dried at 80 °C to harvest $TiO_2/C/MnO_2$. The MnO_2 content could be adjusted by varying the $KMnO_4$ concentration and the catalysts were labeled as TIMP-Mn-x, where X was the concentration of $KMnO_4$, ca 0, 0.005, 0.01, 0.02, 0.05, and 0.1 $moL \cdot L^{-1}$. Scheme 1 vividly describes the synthesis process of $TiO_2/C/MnO_2$ catalysts.

2.2. Activity and stability tests

The photocatalytic mineralization of indoor VOC mixtures (formaldehyde (CH_2O) and toluene (C_7H_8)) was conducted in a quartz glass reactor (1 L). The reactor temperature was kept at constant 25 °C by a simple cooling system and the humidity level was kept at 50% before reaction, which could guarantee to match the practical indoor environment. 0.2 g of photocatalyst was evenly dispersed into deionized water on a quartz glass with a diameter of 7 cm. It was dried in an oven at 60 °C to evaporate water and then placed in the reactor. Subsequently, 2 μL of formaldehyde and 2 μL of toluene were injected into the reactor separately or simultaneously. A xenon lamp with a 420 nm cutoff

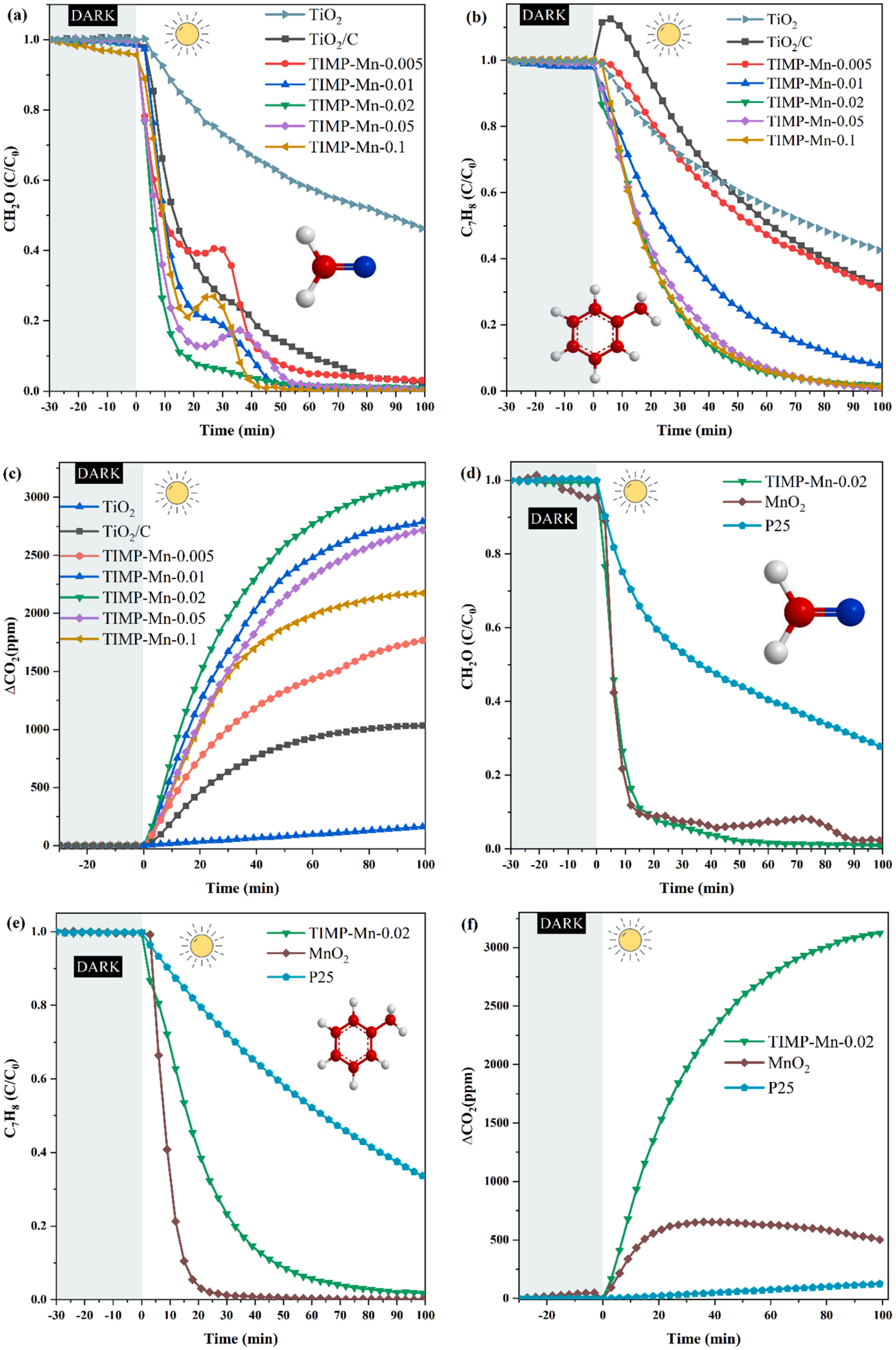

Fig. 1. Photocatalytic degradation performance and CO_2 generation of CH_2O and C_7H_8 mixture under irradiation of xenon lamp with a 420 nm cutoff filter.

filter ($\lambda \geq 420$ nm, 421 $mW \cdot cm^{-2}$) was placed above the quartz glass with a height of 20 cm. Finally, the photocatalytic process was initiated by turning on the lamp after reaching the equilibrium concentration of VOCs. The concentrations of formaldehyde, toluene, and carbon dioxide were monitored online by a photoacoustic infrared multigas monitor (GASERA ONE, Finland). Commercial TiO_2 P25 and MnO_2 were used to compare the mineralization of pollutants with the optimal candidate. The experimental setup is shown in Fig. S1. The difference values of CO_2 with the original concentration in the reactor were labeled as ΔCO_2. The conversion formula of the theoretical gas concentration is as the Eq. (1).

$$C_x = \frac{V_x \times V_m \times \rho \times P_x}{M \times V_r} \tag{1}$$

where C_x is the gas concentration (ppm), V_x is the injection volume of liquid organics, V_m is the molar volume of gas at standard condition, ρ is the density of liquid organics, P_x is the purity of liquid organics, M is the molecular weight, V_r is the volume of the reactor.

The VOCs (CH_2O/C_7H_8) removal efficiency was calculated as Eq. (2).

$$VOC_s conv.(\%) = \frac{[VOC_s] - [VOC_s]_t}{[VOC_s]} \times 100\% \tag{2}$$

2.3. *Catalyst characterization*

The crystal structure of obtained photocatalysts were investigated by an X-ray diffractometer (XRD). The crystal size could be calculated from XRD patterns using the Scherrer formula as Eq. (3). The morphology and microstructure were tested by a field emission scanning electron microscope (SEM) and a high-resolution transmission electron microscope (HRTEM) with a dual-type energy dispersive X-ray spectroscopy (EDX) detector. The chemical states of elements in catalysts were analyzed by an X-ray photoelectron spectroscopy system (XPS). All the binding energies were referred to C 1s at 284.6 eV. The light absorption property was evaluated by UV–vis diffuse reflectance spectrometry spectra (DRS). A fluorescence spectrophotometer ($\lambda ex = 320$ nm) was used to investigate the solid steady-state fluorescence and the transient state fluorescence spectra. In-situ diffuse reflectance infrared Fourier transform spectra (In-situ DRIFTS) were performed to detect the adsorbed species on photocatalyst surface by a Tensor II FT-IR spectrometer. Prior to measurements, the chamber was purged with high purity He. The gas mixture of CH_2O (40 ppm balanced in He), C_7H_8 (40 ppm balanced in He), H_2O, and O_2 was injected into the chamber according to the actual testing requirements. The system humidity level was kept at 50% and the total gas flow rate was set to 100 $mL \cdot min^{-1}$ under visible light. A JES FA200 spectrometer was applied to record the electron spin resonance (ESR) signals of reactive oxygen species (ROS) spin-trapped by 5,5-dimethyl-1-pyrroline N-oxide (DMPO). To detect the byproducts formation during the photocatalytic process, 250 μL of reaction gas was injected into gas chromatography-mass spectrometry (GC-MS) equipped with an automated thermal desorber every 15 min.

$$D = k\lambda/\beta cos\theta \tag{3}$$

where D is the crystal size, k is the shape factor, ca. 0.89, λ is the wavelength of X-ray radiation, β is the FWHM (full width at half maximum) of the corresponding peak, and θ is the angle.

2.4. *Transient breakthrough experiments*

To evaluate the adsorption behavior of the catalyst for CH_2O and C_7H_8 mixture, transient breakthrough experiments were performed. 0.66 g photocatalyst was filled into a cylindrical stainless-steel reactor (i. d. 6.0 mm 3.0 mL volume). The length-diameter ratio of sample loading was 10.0 and the dead volume was 10.0 mL. Prior to the breakthrough measurements, the catalyst was degassed at 105 °C for 120 min with the N_2 gas flow rate of 60 $mL \cdot min^{-1}$. After cooling to room temperature, the gas mixture containing CH_2O, C_7H_8, and N_2 was fed into the bed with a flow rate of 0.165, 0.165, and 162 $mL \cdot min^{-1}$, respectively. The temperature, relative humidity, and pressure were fixed at 25 °C, 50%, and 1.0 bar, respectively. The multi-component mass spectrograph (BSD-MAB) was equipped to continuously monitor each gas concentration. A summary of the transient breakthrough experimental parameters is provided in Table S1. The adsorption capacity calculation formula is presented as Eq. (4):

$$Q_{ads} = V_{total} C_0 \Delta T - \int_0^t \left[V_{N_2} / \left(1 - \sum_1^N C_t \right) \right] C_t dt \tag{4}$$

where Q_{ads} is the adsorption capacity, V_{total} is the total inlet flow rate, C_0 is the initial molar concentration, C_t is the molar concentration at time t, ΔT is the total test time and V_{N_2} is the flow rate of carrier gas.

The adsorption selectivity can be calculated as Eq. (5).

$$S = \left(\frac{X_{CH_2O}}{Y_{CH_2O}} \right) \tilde{A} \cdot \left(\frac{X_{C_7H_8}}{Y_{C_7H_8}} \right) \tag{5}$$

where S is the adsorption selectivity of CH_2O to C_7H_8, X_{CH_2O} and $X_{C_7H_8}$ are the corresponding mole fractions in adsorbed phase, Y_{CH_2O} and $Y_{C_7H_8}$ are the corresponding mole fractions in bulk gas phase.

3. Results and discussion

3.1. *Photocatalytic degradation of CH_2O and C_7H_8 mixture*

The photocatalytic degradation efficiency of the VOC mixture (CH_2O and C_7H_8) was evaluated in a sealed reactor simulating the indoor environment over synthesized catalysts under visible light. Clearly, the concentration of CH_2O, C_7H_8 and CO_2 had stayed almost stable for all samples under the condition of turning off the light. As shown in Fig. 1(a and b), all these catalysts from the IMPs-assisted solvothermal method exhibited superiority on CH_2O and C_7H_8 degradation compared with TiO_2. MnO_2 decoration further promoted degradation within a shorter time, i.e., a higher degradation rate. Interestingly, the CH_2O concentration increased in reaction time between 20 and 35 min for TIMP-Mn-0.1, TIMP-Mn-0.05, TIMP-Mn-0.01 and TIMP-Mn-0.005. This is due to photocatalytic oxidation reactions of C_7H_8 and CH_2O are exothermic radical reactions. In the first 20 min, the faster reaction rate generated a lot of heat in a short time and the decrease of pollutant concentration. If the photocatalytic oxidation capacity and selective adsorption capacity of the catalyst are insufficient, it will lead to the desorption of CH_2O. In comparison, TIMP-Mn-0.02 displayed as the optimal candidate that attained almost complete removal of CH_2O and C_7H_8 after 60 min without the phenomenon of CH_2O desorption. Fig. 1(c) presents CO_2 generation during the photocatalytic degradation process over different catalysts, which reflects the mineralization efficiency. Clearly, negligible CO_2 was observed over pristine TiO_2, indicating incomplete degradation of VOCs with large amounts of organic byproducts. IMPs assistance (TiO_2/C) successfully improved further transformation of intermediates, thus generating more CO_2. Next, MnO_2 decoration on TiO_2/C further boosted deep oxidation and the ΔCO_2 finally reached 3100 ppm for TIMP-Mn-0.02, which was nearly close to the theoretical value, ca. 3844 ppm. In addition, the CH_2O degradation process on TIMP-Mn-0.02 didn't show the phenomenon of CH_2O desorption. This remarkable performance illustrated that TIMP-Mn-0.02 had remarkable photocatalytic oxidation capacity. Nevertheless, further adding MnO_2 decoration amount brought inconspicuously or even deactivated performance on CH_2O and C_7H_8 conversion efficiency. The final CO_2 production consequently fell to 2100 ppm. This may be due to the redox reaction between $KMnO_4$ and C that produced excess MnO_2 with too much consumption of C, blocking the active sites and the decrease of light absorption of photocatalysts [8]. Fig. 1 (d–f) compare the photocatalytic performance between TIMP-Mn-0.02, commercial TiO_2 P25,

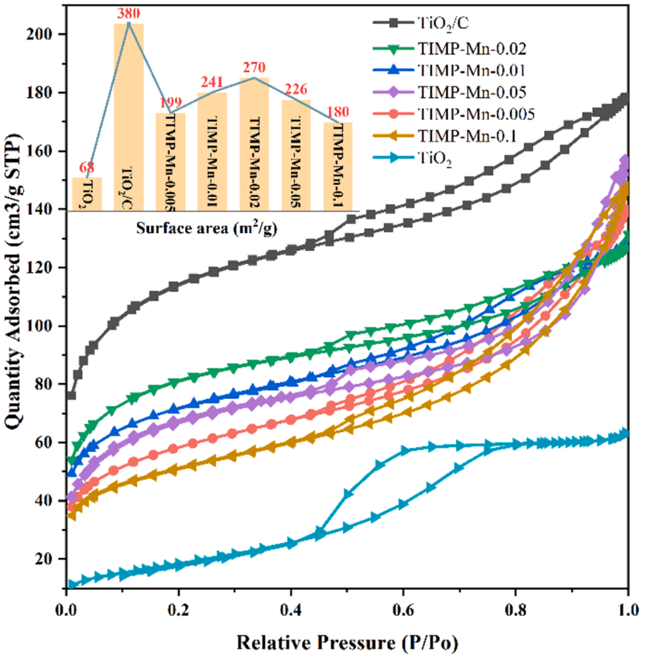

Fig. 2. N_2 adsorption–desorption isotherms and surface area data of TiO_2, TiO_2/C, and TIMP-Mn-0.02.

and MnO_2. TiO_2 P25 exhibited very poor degradation behavior for both CH_2O and C_7H_8, which only reached 70% and 65% conversion, respectively. Moreover, negligible CO_2 was generated for TiO_2 P25. Interestingly, commercial MnO_2 showed similar CH_2O conversion and even higher C_7H_8 conversion compared with TIMP-Mn-0.02. However, the total CO_2 generation only reached approximately 500 ppm for commercial MnO_2, which was significantly lower than that of TIMP-Mn-0.02. Therefore, TIMP-Mn-0.02 not only exhibited excellent photocatalytic conversion efficiency for both CH_2O and C_7H_8 in the VOC mixture but also achieved almost completely mineralization. This outstanding performance was distinctly superior to commercial TiO_2 P25 and MnO_2. The cycle performance of TIMP-Mn-0.02 was evaluated for 5 cycles to investigate its recyclability. The spent catalyst was loaded into the reactor again for the next cycle without any treatment. Fig. S2 demonstrates that both the degradation efficiency of CH_2O and C_7H_8 was almost unchanged after 5 cycles. In conclusion, TIMP-Mn-0.02 with IMPs from waste shell as templates and carbon source showed a remarkable photocatalytic performance and recyclability for VOC mixture mineralization.

3.2. Electronic structure characterization

All these obtained catalysts exhibited anatase TiO_2 diffraction peaks as observed in Fig. S3. There was no obvious MnO_2 peak in all samples, indicating MnO_2 was highly dispersed or presented as large amorphous particles [27]. All these TiO_2/C/MnO_2 catalysts possessed wider FWHMs than TiO_2 (Table S2). Accordingly, the grain sizes of TiO_2/C/MnO_2 were much smaller than that of TiO_2 and TIMP-Mn-0.02 had the smallest grain size (9.00 nm), thus contributing to its high adsorption capacity [28]. Besides, all these catalysts from IMPs-assisted solvothermal method possessed much higher lattice strain than pristine TiO_2, which should attribute to lattice distortion (Table S2). Brunauer Emmett Teller (BET) surface area analysis is shown in Fig. 2, TiO_2/C had the largest surface area, but the introduction of MnO_2 decreased the surface area of photocatalysts dramatically from 380 (TiO_2/C) to 199 $m^2 \cdot g^{-1}$ (TIMP-Mn-0.005). That's because $KMnO_4$ consumed amount of C and the generated MnO_2 had small quantity and low crystallinity due to the low concentration of $KMnO_4$. Subsequently, the surface area of photocatalysts demonstrated first an increase from 199 (TIMP-Mn-0.005) to 270 (TIMP-Mn-0.02) $m^2 \cdot g^{-1}$ and then a decrease from 270 (TIMP-Mn-0.02) to 180 $m^2 \cdot g^{-1}$ (TIMP-Mn-0.1) with the increasing MnO_2 decoration amount. All of the above photocatalysts exhibited larger surface area than pristine TiO_2. The generated MnO_2 nanosheets could increase the surface area of photocatalysts but too much MnO_2 could lead to agglomeration and compaction which had negative effects on the surface area. The morphologies of synthesized catalysts by SEM could also illustrate that. As shown in Fig. 3(a–g), TiO_2 and TiO_2/C processed smooth microspherical morphology. MnO_2 decoration destroyed the structure that exhibited rough and flake surface on the sphere. As the concentration of $KMnO_4$ participation in synthetic reaction was increased, the outer in-situ-grown MnO_2 nanosheets grew thicker and the crystallinity increased. TIMP-Mn-0.02 had the best morphological structure, MnO_2 nanosheets distributed evenly and loosely on the surface of photocatalyst. However, further adding MnO_2 decoration amount caused agglomeration and compaction on the surface. When the concentration of $KMnO_4$ rose to 0.1 moL·L^{-1}, the thickness of MnO_2 on the surface of TIMP-Mn-0.1 was 267 nm as shown in Fig. 3h. Excessively thick MnO_2 layer meant too much consumption of C, blocking the active sites of TiO_2, the decrease of light absorption of photocatalysts and smaller surface area.

To further explore the lattice structure and element distribution in TIMP-Mn-0.02, TEM and EDX mapping of a microsphere were collected as shown in Fig. 4(a) and (b) and Fig. S4. Clearly, Ti was the most abundant element, while Mn, C, and N were uniformly dispersed. TiO_2, C, and MnO_2 were evenly distributed in the composite and formed space net structure. Interestingly, N element from IMPs successfully remained in TIMP-Mn-0.02 with similar distribution to C. Abundant N distribution in the carbon material was beneficial to change the surface basicity and

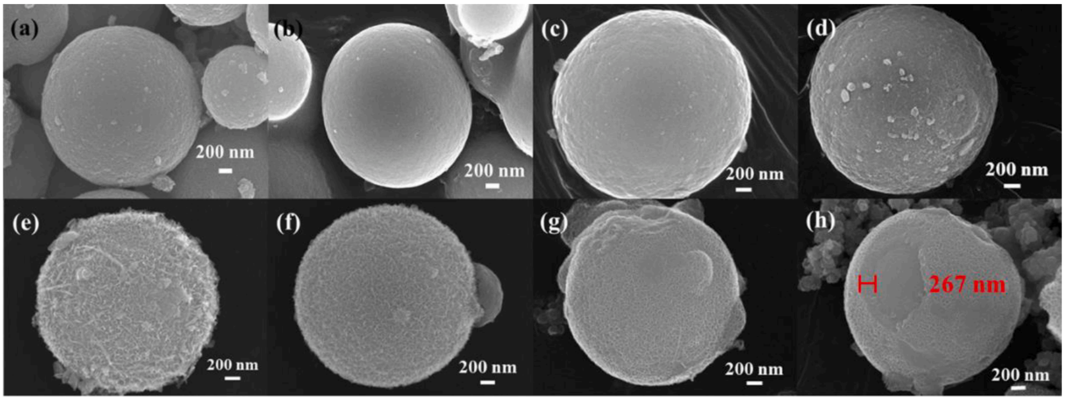

Fig. 3. SEM images of (a)TiO_2, (b) TiO_2/C, (c) TIMP-Mn-0.005, (d) TIMP-Mn-0.01, (e) TIMP-Mn-0.02, (f) TIMP-Mn-0.05, (g) TIMP-Mn-0.1, (h) TIMP-Mn-0.1.

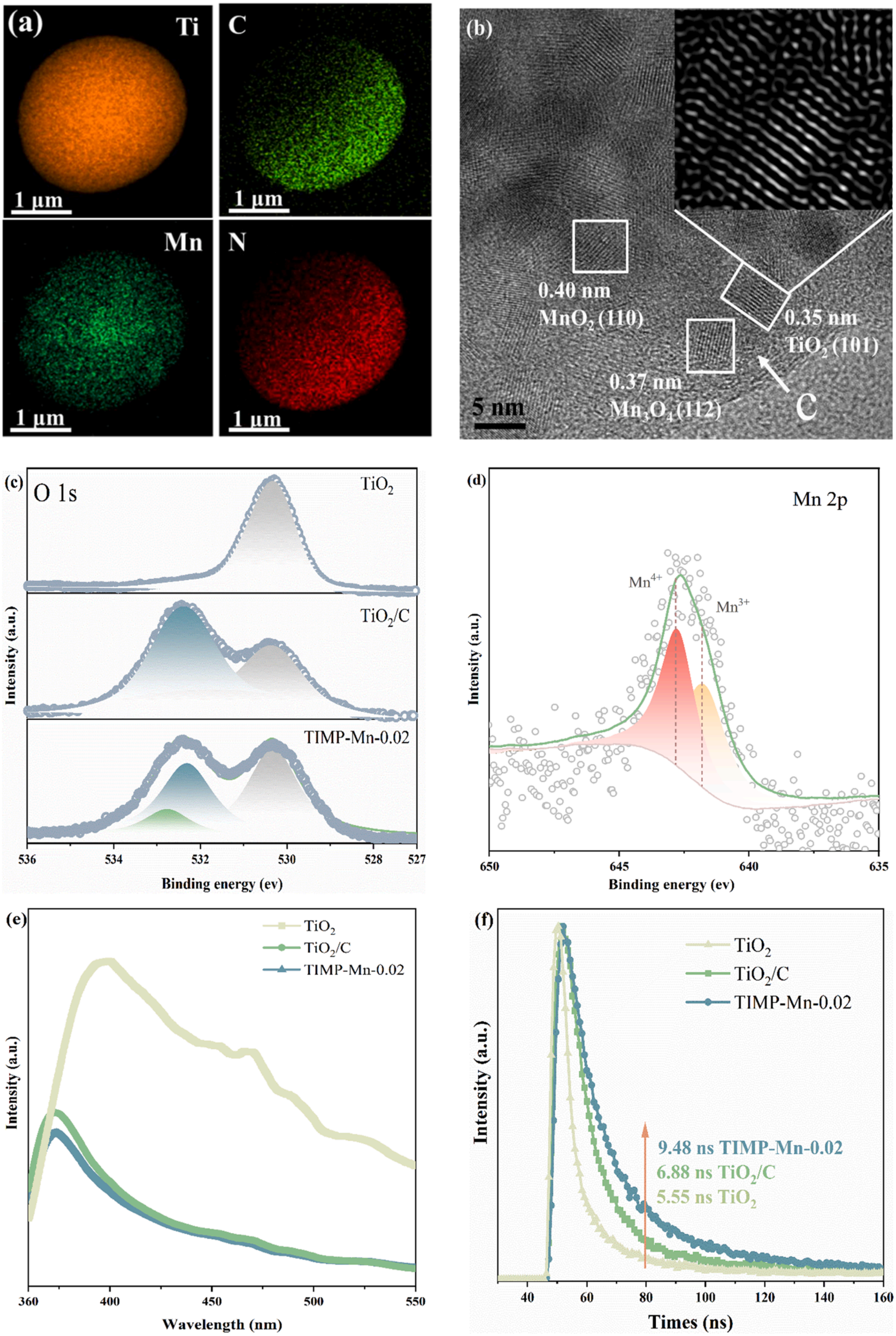

Fig. 4. (a) EDX elemental mapping profiles and (b) HRTEM image of TIMP-Mn-0.02. (c) O 1s XPS of TiO_2, TiO_2/C and TIMP-Mn-0.02. (d) Mn 2p XPS of TIMP-Mn-0.02. (e) Room temperature photoluminescence spectra. (f) Time-resolved photoluminescence decay spectra of TiO_2, TiO_2/C and TIMP-Mn-0.02.

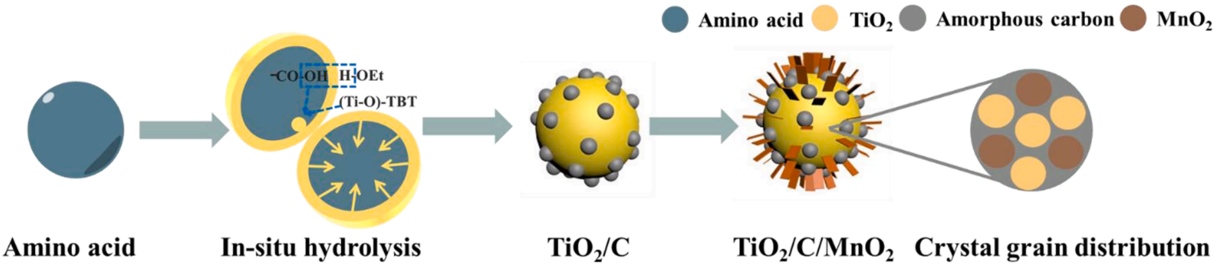

Scheme 2. Illustration of $TiO_2/C/MnO_2$ synthesis process from amino acid in IMPs and $KMnO_4$ decoration.

polarity of catalyst, thus contributing to excellent adsorption performance for VOC molecules with acidity [29,30]. The high-resolution TEM image of TIMP-Mn-0.02 exhibited a regular arrangement of TiO_2, MnO_2, and the amorphous carbon between crystals [31]. Besides, the Fourier filtered crystal of TiO_2 showed severe lattice distortions that was consistent with the increased lattice strain calculated from XRD. These lattice distortions should originate from abundant oxygen vacancies and Ti^{3+} ions, inducing valence band tail to tailor the bandgap structure and enhance the visible light absorption [28]. XPS analysis was adapted to investigate the composition and valence state of surface elements. Fig. S5 shows the C 1s XP spectra of TiO_2/C and TIMP-Mn-0.02, which exhibited negligible difference. Three peaks at approximately 284.8, 286.1, and 288.8 eV were ascribed to C—C, C—O, and C—N bonds, respectively [32,33]. There was no obvious difference in N 1s XP spectra between TiO_2/C and TIMP-Mn-0.02, and the peak at the highest binding energy of 398 eV represented the C—N bond (Fig. S6) [34]. The results of C 1s and N 1s XP spectra proved the presence of amorphous C and N distribution in the carbon material. As shown in Fig. 4(c), large amounts of oxygen vacancies (O_V) as the strong peak centralized at 532.3 eV of TiO_2/C, while pristine TiO_2 possessed dominant lattice oxygen species

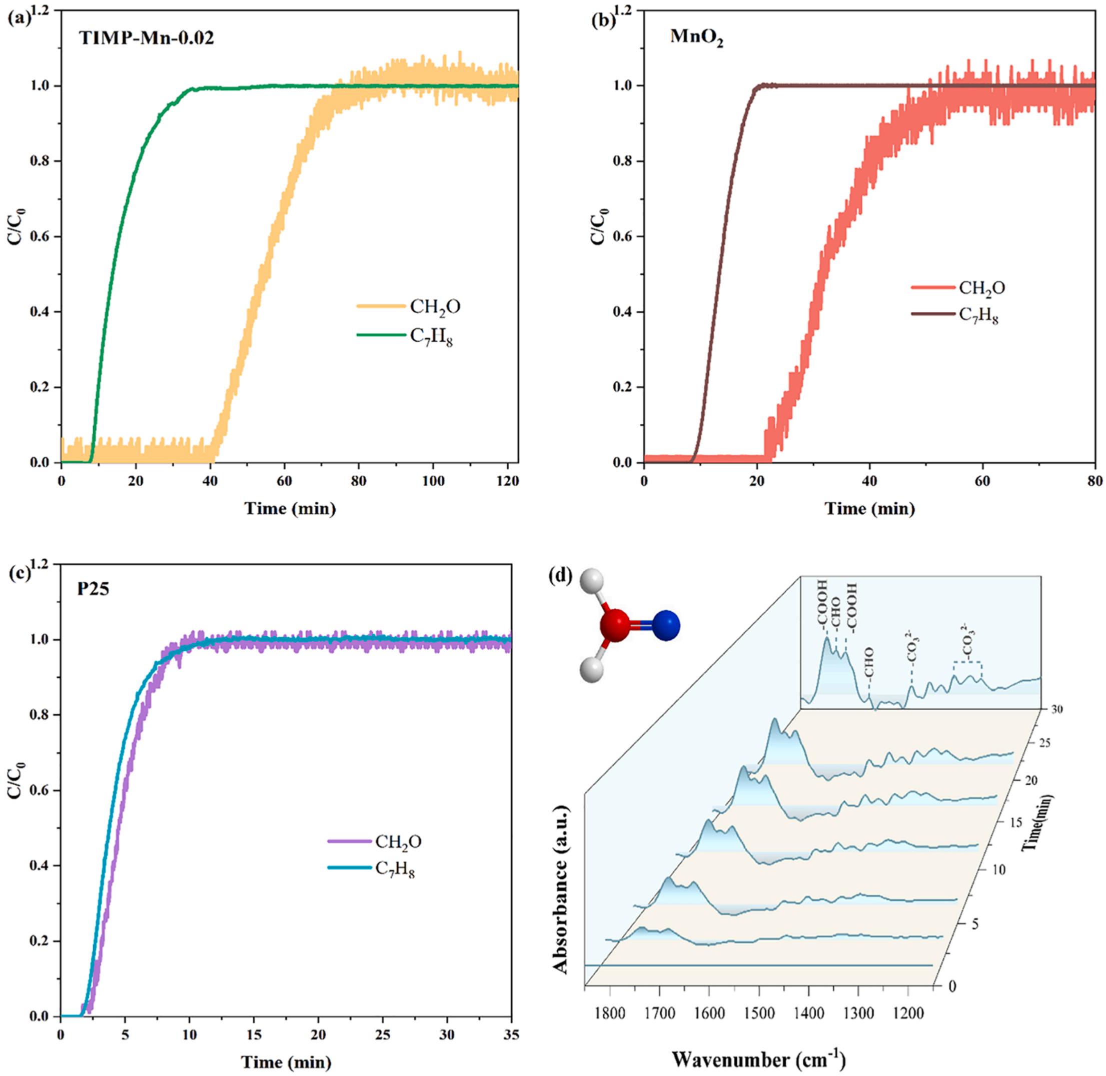

Fig. 5. Adsorption breakthrough curve of an isoconcentration CH_2O and C_7H_8 mixture through (a) TIMP-Mn-0.02, (b) MnO_2 and (c) P25 at 25 °C, 50% humidity and 1.0 bar. In situ DRIFTS measurements of (d) single CH_2O, (e and f) single C_7H_8 and (g and h) CH_2O and C_7H_8 mixture for the detection of adsorbed species on the TIMP-Mn-0.02 surface in dark.

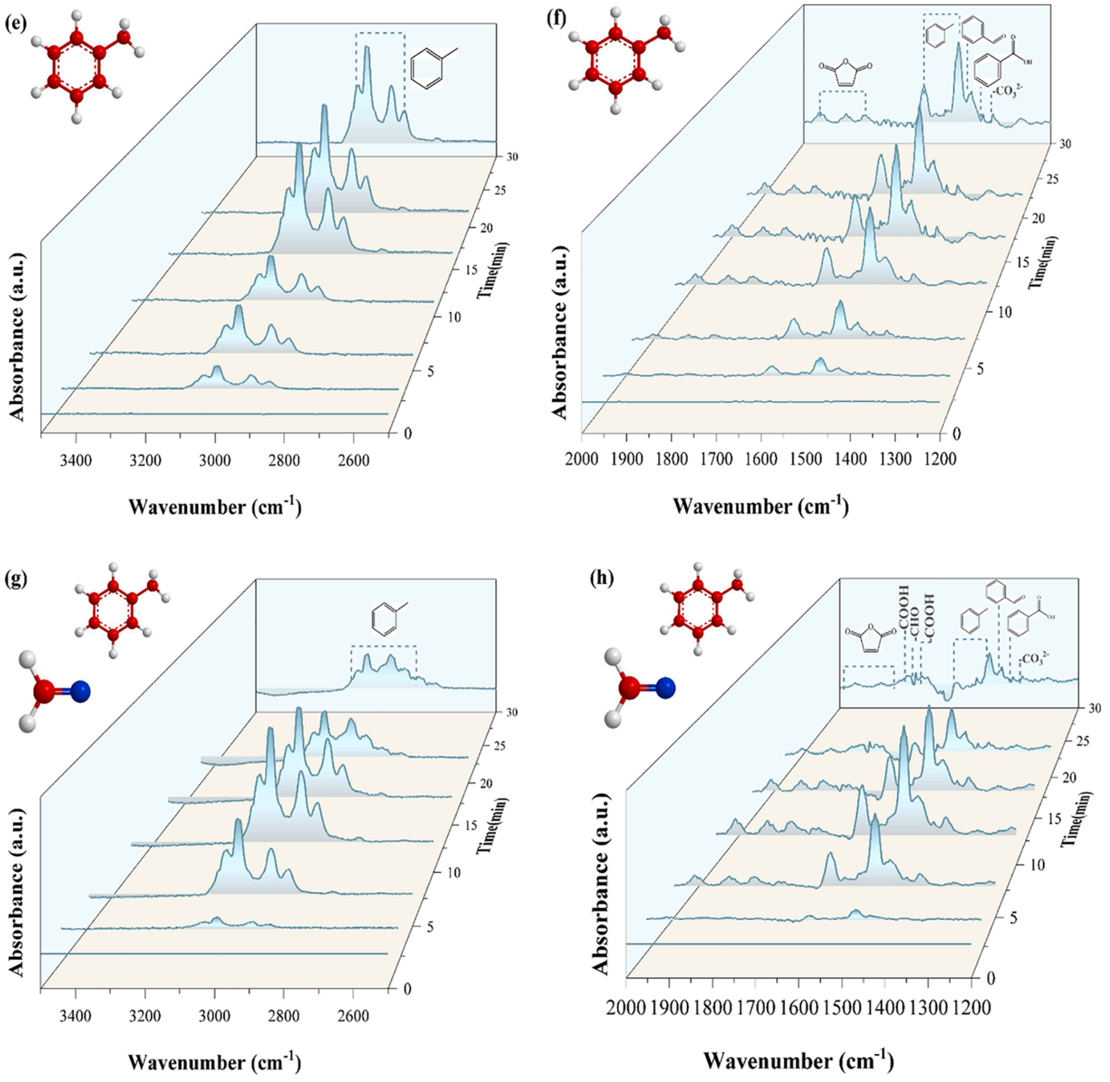

Fig. 5. (*continued*).

(O_l) located at 530.4 eV with a slight amount of O_v. TIMP-Mn-0.02 with MnO_2 decoration had three types of oxygen species that the adsorbed oxygen species (O_a) emerged at 532.7 eV expect for O_v and O_l, confirming the enhancement of adsorption for ROS and the existence of abundant oxygen vacancies [35]. The Mn 2p spectra shown in Fig. 4(d) depicted the co-existence of Mn^{4+} and Mn^{3+} as the two peaks located at 642.7 and 641.7 eV in the region of Mn $2p_{3/2}$ [36–38]. The proportion of Mn^{3+}/Mn^{4+} was calculated to be 1:1 based on the integrated area. The presence of Mn^{3+} validated the existence of oxygen vacancies for maintaining electrostatic balance, which was important for the photocatalytic oxidation capacity of catalyst [39].

The light absorption capacity of catalysts with different MnO_2 contents was investigated by UV–vis diffuse reflectance spectroscopy (DRS) (Fig. S7–S8). Pristine TiO_2 could only absorb the light with wavelength ranging from 200 to 400 nm. Apparently, TiO_2/C and all these $TiO_2/C/MnO_2$ catalysts could absorb the light in the whole visible region. Therefore, C introduction from IMPs effectively promoted full spectral absorption of TiO_2. Besides, TiO_2/C exhibited a groove ranging in 200 ~ 340 nm, i.e., UV region absorption, but it elevated gradually with increasing of MnO_2 content. Higher MnO_2 content implied more $KMnO_4$ dosage, therefore more C was consumed in IMPs to expose more TiO_2 on the catalyst surface. The optical bandgap was calculated based on DRS results and listed in Table S2. TiO_2/C and $TiO_2/C/MnO_2$ exhibited lower bandgap than pristine TiO_2. In comparison, TIMP-Mn-0.02 had the minimum bandgap, ca. 1.9 eV. The narrower band gap was consistent with the fact that TIMP-Mn-0.02 could absorb more photons [40] and generate electron holes more easily [21]. Fig. 4(e) shows that the PL intensity of TIMP-Mn-0.02 was much lower than that of TiO_2 and TiO_2/C, demonstrating enhanced separation and reduced recombination of charge carriers. The transient time-resolved fluorescence tests further confirmed the retarded recombination of charge carriers over TIMP-Mn-0.02, as shown in Fig. 4(f). The average lifetime of charge carriers was approximately 9.48 ns for TIMP-Mn-0.02, which was much longer than that of TiO_2 (5.55 ns) and TiO_2/C (6.88 ns). The electrochemical impedance spectroscopy (EIS) and transient photocurrent were employed to further confirm the migration and spatial redistribution of charge carriers. In Fig. S9, it's clear that TIMP-Mn-0.02 had a smaller semicircular diameter compared with TiO_2 and TiO_2/C, and it exhibited higher photocurrent density in Fig. S10. These results indicated that TIMP-Mn-0.02 possessed lower charge-transfer resistance and less charge recombination [41–43], confirming the super photocatalytic activity of TIMP-Mn-0.02.

3.3. *In-depth mechanism of photocatalytic CH_2O and C_7H_8 mixture degradation*

Scheme 2 illustrates the $TiO_2/C/MnO_2$ synthesis process. IMPs broke down into insoluble amino acids in ethanol [1,25]. Amino acids were

Table 1
The summary of the transient breakthrough results in TIMP-Mn-0.02.

Composition	Breakthrough point (5%) min	Half dry point (50%) min	Dry point (95%) min	Saturated adsorption capacity mL·g^{-1}	Separation rate of CH_2O to C_7H_8
CH_2O	43.4	54.1	68.7	13.7	3.5
C_7H_8	6.8	13.7	28.8	3.9	

utilized as effective template to synthesize catalyst precursor and evenly distributed in the precursor. After calcination in an anaerobic atmosphere, C was distributed in TiO_2. In the next process, $KMnO_4$ was reduced to by C: $4MnO_4^- + 3C + H_2O = 4MnO_2 + CO_3^{2-} + 2HCO_3^-$ [44]. Due to the distribution character of C, the generated MnO_2 was evenly distributed throughout the sphere, not only the outer flake of the catalyst but also the inner flake. Because of this particular structure, C atoms were hard to be reduced thoroughly and forming $TiO_2/C/MnO_2$ without the C coating step. This well-constructed hybrid architecture enhanced the stability and electron transport throughout the composite catalyst.

The transient breakthrough experiments were carried out to evaluate the competitive adsorption behavior of the catalyst for CH_2O and C_7H_8 mixture. As shown in Fig. 5(a), at the same condition, C_7H_8 first eluted through the fixed bed in a short time, whereas TIMP-Mn-0.02 retained CH_2O. C_7H_8 at the outlet of column rapidly increased to half dry point at 13.7 min, while the time of CH_2O was 54.1 min. The saturation adsorption time (dry point) of catalyst for CH_2O and C_7H_8 were 68.7 and 28.8 min, respectively. From the calculations using the transient breakthrough results of Fig. S11, the maximum adsorption capacity of CH_2O was significantly higher than that of C_7H_8, ca. 13.727 > 3.961 mL·g^{-1}. Table 1 provided a summary of the transient breakthrough results. This might explain that the CH_2O molecules had much stronger adsorption strength than C_7H_8 in TIMP-Mn-0.02 and they gradually occupied most of the possible adsorption site. Compared with TIMP-Mn-0.02, the interval of CH_2O and C_7H_8 breakthrough points on MnO_2 and P25 were shorter, 12.4 and 0.47 min, respectively (Fig. 5(b and c)). In addition, large difference of adsorption capacity may also promise in separating CH_2O and C_7H_8 [45]. But these differences on MnO_2 and P25 were only ~3.6 and 0.2 mL/g, which were well below that of TIMP-Mn-0.02 (~9.8 mL·g^{-1}), as shown in Table S3 and S4. The separation rate of C_7H_8 to CH_2O could reflect the adsorption selectivity of catalysts directly. TIMP-Mn-0.02 had 8.5 and 3.9 times the separation rate of MnO_2 and P25, respectively. Hence, TIMP-Mn-0.02 had the best adsorption selectivity and these results complied with the degradation experiments. The considerable difference of adsorption rate (Fig. S12)

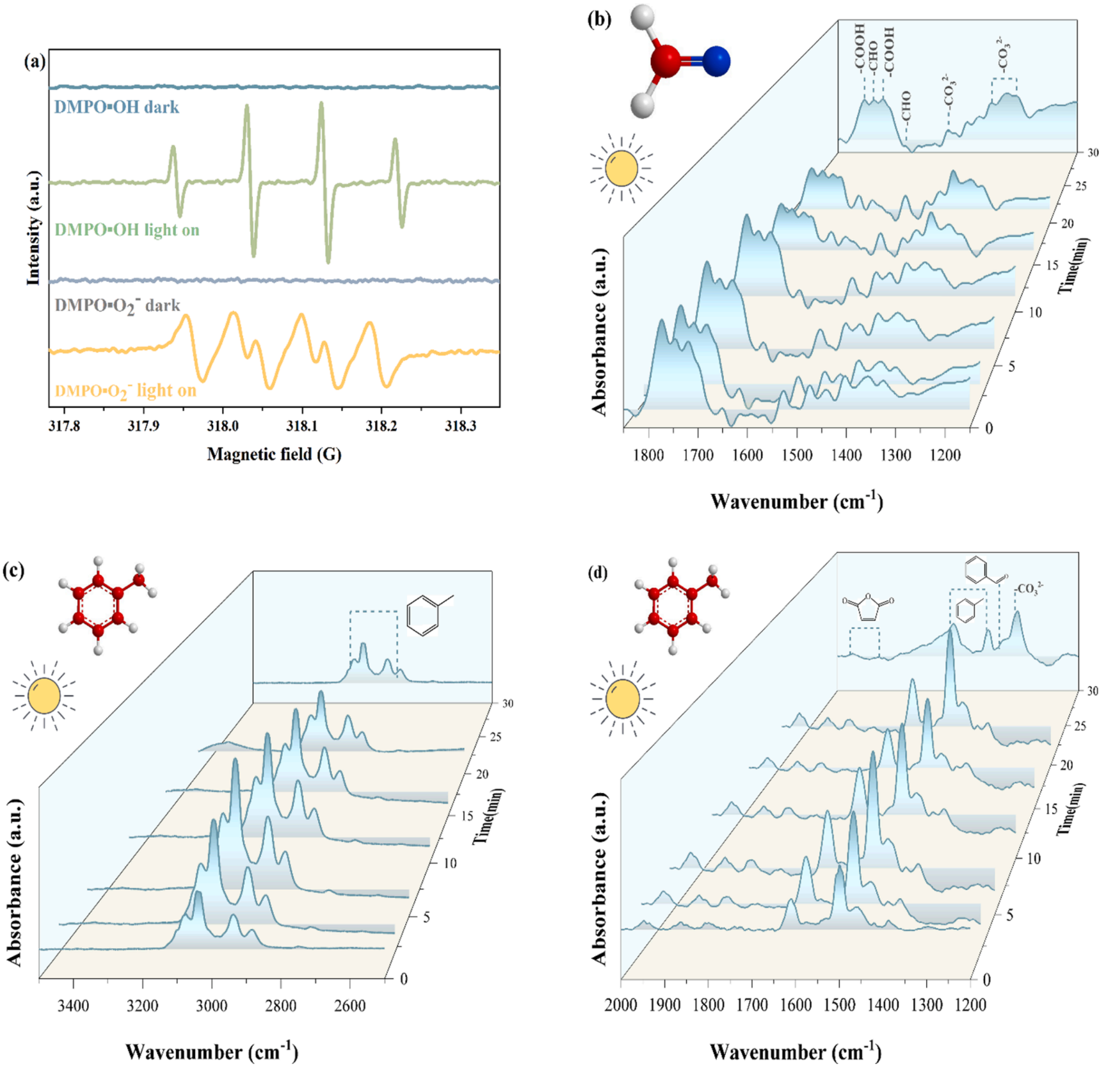

Fig. 6. (a) ESR spectra of TIMP-Mn-0.02 in the presence of DMPO as radical scavenger: DMPO•O_2^- and DMPO•HO. In situ DRIFTS measurements of (b) single CH_2O, (c and d) single C_7H_8 and (e and f) CH_2O and C_7H_8 mixture for the detection of adsorbed species on the TIMP-Mn-0.02 surface under visible light. (g and h) The photocatalytic decomposition efficiency of the single target VOC components (CH_2O, C_7H_8) and their mixture.

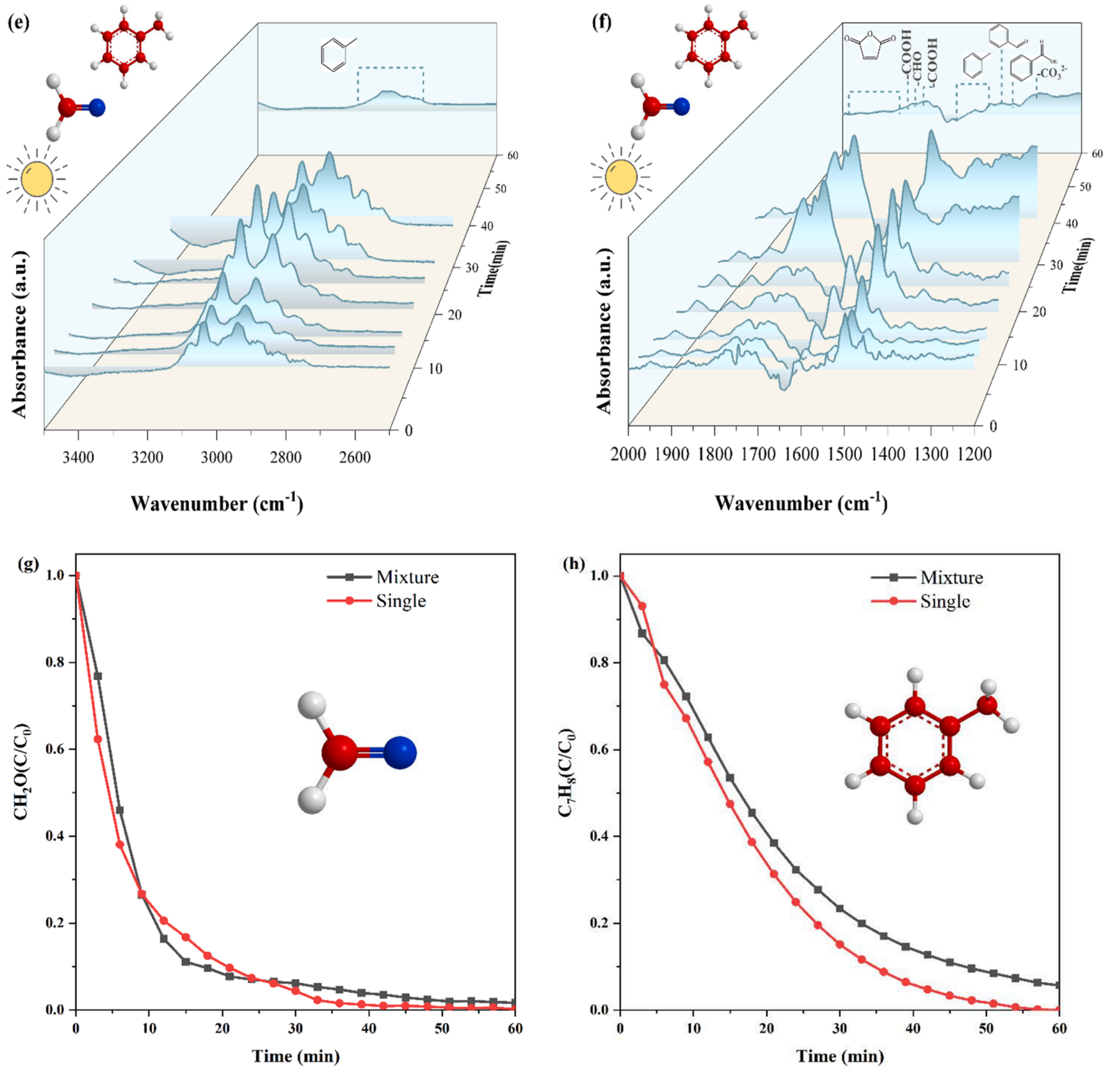

Fig. 6. (*continued*).

and high separation rate of TIMP-Mn-0.02 indicated that CH_2O preferentially adsorbed on the catalyst and could be rapidly mineralized because of its high photocatalytic oxidation capacity, avoiding the addition reactions between CH_2O and C_7H_8 and improving the mineralization ratio of the gas mixture.

In-situ DRIFTS measurements were applied to further study the adsorption behavior of the TIMP-Mn-0.02 for CH_2O and C_7H_8 mixture during dark adsorption. Firstly, the adsorption of single gas was measured as benchmark. As depicted in Fig. 5(d), under the circumstance of CH_2O adsorption, $-$CHO (1646 and 1745 cm^{-1}) [46,47], $-$COOH (1718 and 1772 cm^{-1}) [47,48], and $-$ CO_3^{2-} (1347 – 1408 cm^{-1}) [49,50] were observed, which were indexed as formaldehyde, formic acid, and carbonic acid, respectively. For C_7H_8 single adsorption, the strong bands at 2800 – 3100 and 1495 – 1600 cm^{-1} belonged to C—H groups and the benzene ring in-plane and out-plane deformations vibration were attributed to C_7H_8 [51]. The weak bands at 1457, 1419, 1800 – 1958, and 1388 cm^{-1} were corresponding to benzaldehyde [5], benzoic acid [5], maleic anhydride [52], and carbonic acid [46], respectively (Fig. 5(e and f)). All these bands were strengthened with prolonging adsorption time. Co-adsorption of CH_2O and C_7H_8 did not generate new bands that were not observed during single adsorption. The bands climbed gradually within the first 15 min. Next, only the bands originating from CH_2O continued to strengthen, while the C_7H_8 related bands were dramatically weakened, as shown in Fig. 5(g and h). This illustrated that the CH_2O molecules might have a competitive adsorption behavior over C_7H_8 when the available adsorption sites in TIMP-Mn-0.02 decreased, hence, leading to a decrease of C_7H_8. This inference was in accordance with transient breakthrough results.

In the synthesis process, the catalyst was prepared in an oxygen-deficient atmosphere, contributing to more oxygen vacancies [28]. The existence of oxygen vacancies had been confirmed by XRD, HRTEM and XPS, suggesting that the generation ROS played an important role in photocatalytic degradation. ESR spectroscopy was performed to validate the existence of ROS for the enhanced photocatalytic performance. As shown in Fig. 6(a), there were no DMPO•O_2^- and DMPO•OH characteristic signals under darkness. After turning on the visible light, the typical peaks corresponding to DMPO•O_2^- and DMPO•OH were observed [53]. The ESR results further validated that •OH and •O_2^- were generated on TIMP-Mn-0.02 surface under visible light, resulting in intensive CH_2O and C_7H_8 mixture gas degradation efficiency.

In-situ DRIFTS measurements under visible light irradiation were applied to further explore the degradation mechanism of CH_2O and C_7H_8 mixture over TIMP-Mn-0.02. As the photocatalytic degradation of CH_2O proceeded individually, the typical peaks in the adsorption process still existed during the whole photocatalytic process in Fig. 6(b). The $-$COOH exhibited an increase in the first 10 min and obviously dropped in the remaining time. On the contrary, $-CO_3^{2-}$ varied oppositely and accumulated on the surface of TIMP-Mn-0.02, indicating H_2CO_3 self-

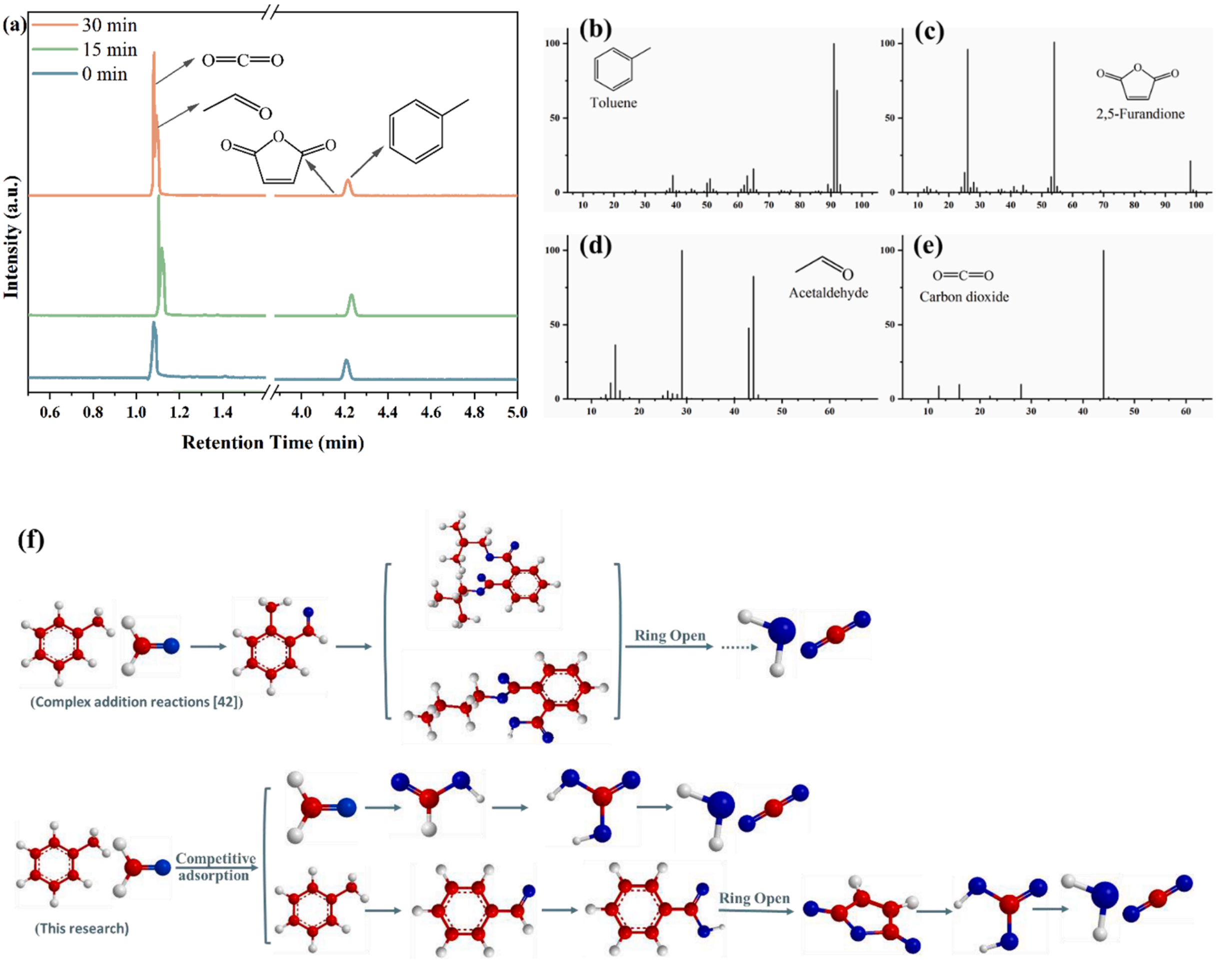

Fig. 7. (a) GC-MS chromatograms with a prolonged time on TIMP-Mn-0.02 for the determination of reaction intermediates in the gas-phase photocatalytic decomposition of CH_2O and C_7H_8 mixture. Typical compounds (b) toluene, (c) 2,5-furandione, (d) acetaldehyde and (e) carbon dioxide from the outlet gas of reactor determined by GC-MS during the photocatalytic degradation of CH_2O and C_7H_8 mixture. (f) Possible photocatalytic oxidation reaction routes for CH_2O and C_7H_8 mixture.

decomposition should be the rate-determining step. The primary pathway could be inferred as HCHO → HCOOH → H_2CO_3 → $CO_2 + H_2O$. Under the circumstance of C_7H_8 degradation (Fig. 6(c and d)), the accumulated C_7H_8 was oxidized to benzaldehyde, benzoic acid, maleic anhydride, and carbonic acid, which were finally mineralized into H_2O and CO_2. TIMP-Mn-0.02 had high photocatalytic ability in C_7H_8 degradation, which had the same rate-determining step with CH_2O degradation and the main pathway took place as following steps: toluene → benzaldehyde → benzoic acid → maleic anhydride → carbonic acid → $CO_2 + H_2O$. In the case of the CH_2O and C_7H_8 mixture (Fig. 6(e and f)), similar reaction processes were noted for CH_2O and C_7H_8 in comparison with single component. But the degradation rate of CH_2O in the mixture was close to that of single CH_2O degradation in the first 30 min, and then become lower in the next 30 min. This is because the too low concentration of CH_2O made it lose advantages in competitive adsorption. For C_7H_8 degradation, the degradation rate of C_7H_8 in the mixture was lower in comparison with the single C_7H_8 in the whole process. To drive home the point, experiments were designed to compare the degradation efficiencies of the mixture and single contaminants on TIMP-Mn-0.02 as shown in Fig. 6(g and h). In addition, the CO_2 generation of single CH_2O and single C_7H_8 were combined to compare with that of the mixture (Fig. S13). The total CO_2 generation of single contaminants were higher than that of the mixture in the same reaction time, side confirming the above results. These results complied with the in-situ DRIFTS results. Comfortingly, the ring-opening process of C_7H_8 was still observed, with maleic anhydride and carbonic acid gradually increased on the catalyst as the reaction proceeded. Especially in the 60 min, almost all the signals corresponding to CH_2O, C_7H_8, and other intermediate products trailed away to disappear except for a little carbonic acid remaining. Furthermore, gas chromatography-mass spectrometry (GC-MS) was applied to monitor the intermediates in the gas (Fig. 7(a–e)). Toluene, 2,5-furandione, acetaldehyde, and carbon dioxide were also found with the photocatalysis of TIMP-Mn-0.02. Fortunately, complex and macromolecular compounds were not detected [49]. Taking all the intermediates into account, the possible photocatalytic oxidation reaction routes for CH_2O and C_7H_8 mixture are shown in Fig. 7(f). TIMP-Mn-0.02 had strong photocatalytic oxidation for CH_2O and C_7H_8 mixture mineralization and the same pathway compared to the single component.

Based on the above results, the possible adsorption-photocatalysis of mechanism for CH_2O and C_7H_8 mixture mineralization under visible light irradiation was clarified. The composite catalyst was composed of $TiO_{2,}$ C, and MnO_2. The N atoms in carbon materials from amino acids provided additional electrons, inducing surface basicity and abundant oxygen vacancies in catalyst [29]. These advantages were conductive to form superoxide ions with high hydrophilicity [26]. CH_2O and C_7H_8 had different affinity. When the concentration of CH_2O with strong adsorption affinity reached a certain degree, competitive adsorption would occur on the adsorption site to replace C_7H_8 with weak adsorption affinity, avoiding the complex addition reactions between CH_2O and C_7H_8. Under visible light irradiation, the formation of the ternary structure and synergistic effect between TiO_2, MnO_2, and C promoted the generation of ·OH and $\cdot O^{2-}$ radicals and accelerated the mineralization of

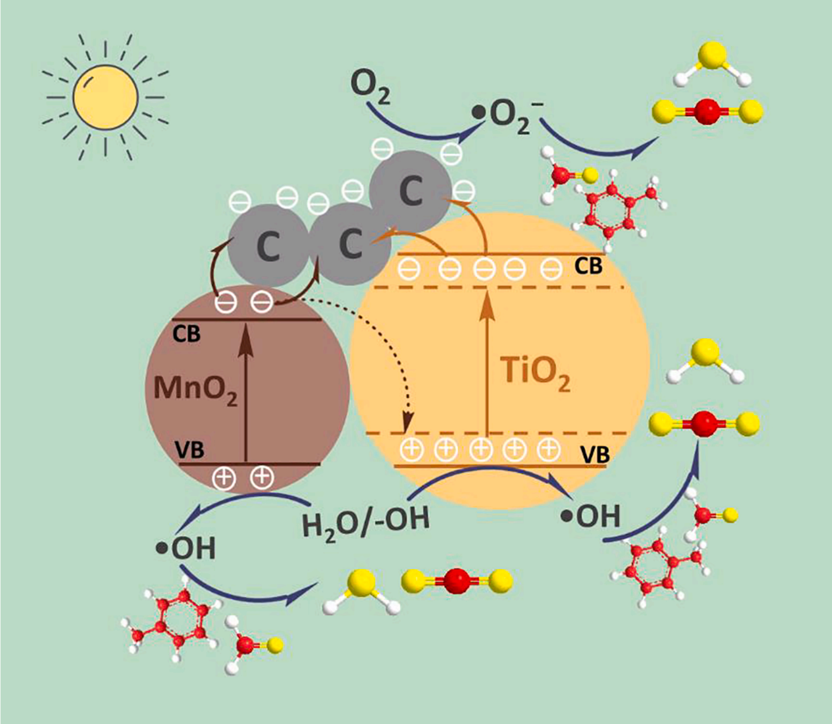

Scheme 3. Proposed mechanism of photocatalytic CH_2O and C_7H_8 mixture degradation over TIMP-Mn-0.02.

CH_2O and C_7H_8 mixture on the composite. As shown in Scheme 3, part of excited electrons in MnO_2 conduction band (CB) can transfer and combine with the holes in TiO_2 valence band (VB). However, the d-π conjugation structure of $TiO_2/C/MnO_2$ promoted electrons transformation from CB of TiO_2 and MnO_2 to C due to its excellent conductivity [28]. This process further promoted the separation of photogenerated electrons and holes, thus prolonging the lifetime of the charge carriers. These electrons and holes can be rapidly caught by O_2 and OH^-/H_2O to generate ·OH and $\cdot O^{2-}$ radicals, respectively. Compared to traditional TiO_2/MnO_2 photocatalyst, carbon materials derived from IMPs contributed to the visible light utilization, special absorption characteristics, effective separation of electron-hole pairs and the enhanced electron transport throughout the photocatalyst of $TiO_2/C/MnO_2$ composite. Thus, this ternary structure significantly improved the photocatalytic degradation effect of VOCs mixture.

4. Conclusions

Natural material insoluble matrix proteins extracted from abalone shell waste serve as carbon source was used to synthesize a kind of unique ternary structure $TiO_2/C/MnO_2$ composite which TiO_2, C and MnO_2 were evenly distributed in the composite and formed space net structure through a handy, sustainable and green method. TIMP-Mn-0.02 exhibited outstanding photocatalytic activity for indoor CH_2O and C_7H_8 mixture mineralization at room temperature under visible light irradiation, achieving near completely mineralization CH_2O and C_7H_8 mixture within 60 min and exhibited remarkable stability after 5 cycles. Characterization results indicated that TIMP-Mn-0.02 had narrower optical band gap and longer lifetime charge carriers, because of the lattice distortions which can induce a valence band tail and d-π conjugation structure of $TiO_2/C/MnO_2$ allowed electrons to transfer from CB of TiO_2 and MnO_2 to carbon, respectively. The transient breakthrough experiments, in-situ DRIFTs and GC-MS were applied to explore the mechanism, the results revealed that this kind of photocatalyst had high adsorption selectivity and strong photocatalytic oxidation for CH_2O and C_7H_8 mixture mineralization. When competitive adsorption occurred, CH_2O with strong adsorption affinity would replace C_7H_8 with weak adsorption affinity on the adsorption site and could be mineralized rapidly avoiding addition reactions and producing potentially toxic and refractory intermediates. This work provided a creative and facile way from synthesization super photocatalyst to resolve severe seashell waste and indoor VOC mixture pollution problems.

Declaration of Competing Interest

The authors declare that they have no known competing financial interests or personal relationships that could have appeared to influence the work reported in this paper.

Acknowledgment

This work was supported by the National Key Research and Development Program of China (2019YFC1903903), Young Elite Scientists Sponsorship Program by Tianjin (TJSQNTJ-2020-13), and Tianjin Science and Technology Project (18YFJLCG00090).

Appendix A. Supplementary data

Supplementary data to this article can be found online at https://doi.org/10.1016/j.cej.2021.131678.

References

[1] W. Wang, H. Yu, K. Li, F. Lin, C. Huang, B. Yan, Z. Cheng, X. Li, G. Chen, L.-a. Hou, Insoluble matrix proteins from shell waste for synthesis of visible-light response photocatalyst to mineralize indoor gaseous formaldehyde, J. Hazard. Mater. 415 (2021) 125649, https://doi.org/10.1016/j.jhazmat.2021.125649.

[2] Z. Wang, H. Yu, Y. Xiao, L. Zhang, L. Guo, L. Zhang, X. Dong, Free-standing composite films of multiple 2D nanosheets: Synergetic photothermocatalysis/photocatalysis for efficient removal of formaldehyde under ambient condition, Chem. Eng. J. 394 (2020) 125014, https://doi.org/10.1016/j.cej.2020.125014.

[3] Z. Wang, H. Yu, L. Zhang, L. Guo, X. Dong, Photothermal conversion of graphene/layered manganese oxide 2D/2D composites for room-temperature catalytic purification of gaseous formaldehyde, J. Taiwan Inst. Chem. E. 107 (2020) 119–128, https://doi.org/10.1016/j.jtice.2019.12.005.

[4] Z. Wang, H. Yu, Y. Xiao, L. Guo, L. Zhang, X. Dong, Polydopamine mediated modification of manganese oxide on melamine sponge for photothermocatalysis of gaseous formaldehyde, J. Hazard. Mater. 407 (2021) 124795, https://doi.org/10.1016/j.jhazmat.2020.124795.

[5] W. Qu, P. Wang, M. Gao, J.-y. Hasegawa, Z. Shen, Q. Wang, R. Li, D. Zhang, Delocalization effect promoted the indoor air purification via directly unlocking the ring-opening pathway of toluene, Environ. Sci. Technol. 54 (15) (2020) 9693–9701, https://doi.org/10.1021/acs.est.0c0290610.1021/acs.est.0c02906.s001.

[6] Z. Rao, G. Shi, Z. Wang, A. Mahmood, X. Xie, J. Sun, Photocatalytic degradation of gaseous VOCs over Tm^{3+}-TiO_2: revealing the activity enhancement mechanism and different reaction paths, Chem. Eng. J. 395 (2020) 125078, https://doi.org/10.1016/j.cej.2020.125078.

[7] A. Lu, H. Sun, N. Zhang, L. Che, S. Shan, J. Luo, J. Zheng, L. Yang, D.-L. Peng, C.-J. Zhong, B. Chen, Surface partial-charge-tuned enhancement of catalytic activity of platinum nanocatalysts for toluene oxidation, ACS Catal. 9 (8) (2019) 7431–7442, https://doi.org/10.1021/acscatal.9b0177610.1021/acscatal.9b01776.s001.

[8] Y. Zhang, M. Wu, Y.H. Kwok, Y. Wang, W. Zhao, X. Zhao, H. Huang, D.Y.C. Leung, In-situ synthesis of heterojunction TiO_2/MnO_2 nanostructure with excellent performance in vacuum ultraviolet photocatalytic oxidation of toluene, Appl. Catal. B: Environ. 259 (2019) 118034, https://doi.org/10.1016/j.apcatb.2019.118034.

[9] P. Wei, D. Qin, J. Chen, Y. Li, M. Wen, Y. Ji, G. Li, T. An, Photocatalytic ozonation mechanism of gaseous n-hexane on MOx-TiO_2-foam nickel composite (M=Cu, Mn, Ag): unveiling the role of $^{\cdot}OH$ and $^{\cdot}O^{2-}$, Environ. Sci. Nano. 6 (3) (2019) 959–969, https://doi.org/10.1039/C8EN01291A.

[10] I. Aouadi, J.-M. Tatibouët, L. Bergaoui, MnOx/TiO2 catalysts for VOCs abatement by coupling non-thermal plasma and photocatalysis, Plasma Chem. Plasma P. 36 (2016) 1485-1499. https://doi.org/10.1007/s11090-016-9740-3.

[11] D. Sarkar, K.K. Chattopadhyay, Branch density-controlled synthesis of hierarchical TiO_2 nanobelt and tunable three-step electron transfer for enhanced photocatalytic property, ACS Appl. Mater. Inter. 6 (13) (2014) 10044–10059, https://doi.org/10.1021/am502379q.

[12] I.F. Mironyuk, L.M. Soltys, T.R. Tatarchuk, V.I. Tsinurchyn, Ways to improve the efficiency of TiO_2-based photocatalysts (review), Phys. Chem. Solid State. 21 (2020) 300–311, https://doi.org/10.15330/pcss.21.2.300-311.

[13] M.T. Noman, M.A. Ashraf, A. Ali, Synthesis and applications of nano-TiO_2: a review, Environ. Sci. Pollut. R. 26 (4) (2019) 3262–3291, https://doi.org/10.1007/s11356-018-3884-z.

[14] S. Yu, H.J. Yun, Y.H. Kim, J. Yi, Carbon-doped TiO_2 nanoparticles wrapped with nanographene as a high performance photocatalyst for phenol degradation under visible light irradiation, Appl. Catal. B: Environ. 144 (2014) 893–899, https://doi.org/10.1016/j.apcatb.2013.08.030.

[15] F. Liu, N. Feng, L. Yang, Q. Wang, J. Xu, F. Deng, Enhanced photocatalytic performance of carbon-coated TiO_{2-x} with surface–active carbon species, J. Phys. Chem. C. 122 (20) (2018) 10948–10955, https://doi.org/10.1021/acs.jpcc.8b02716.

[16] J. Di, X. Fu, H. Zheng, Y. Jia, H-TiO_2/C/MnO_2 nanocomposite materials for high-performance supercapacitors, J. Nanopart. Res. 17 (2015) 255, https://doi.org/10.1007/s11051-015-3060-z.

[17] S. Yang, P. Yan, Y. Li, K. Ye, K. Cheng, D. Cao, G. Wang, Q. Li, PPy wrapped MnO_2@C/TiO_2 nanowire arrays for electrochemical energy storage, Electrochim. Acta. 182 (2015) 1153–1158, https://doi.org/10.1016/j.electacta.2015.09.123.

[18] Q. Xiong, C. Zheng, H. Chi, J. Zhang, Z. Ji, Reconstruction of TiO_2/MnO_2-C nanotube/nanoflake core/shell arrays as high-performance supercapacitor electrodes, Nanotechnology 28 (5) (2017) 055405, https://doi.org/10.1088/1361-6528/28/5/055405.

[19] D. Shin, J. Shin, T. Yeo, H. Hwang, S. Park, W. Choi, Scalable synthesis of triple-core-shell nanostructures of TiO_2@MnO_2@C for high performance supercapacitors using structure-guided combustion waves, Small 14 (11) (2018) 1703755, https://doi.org/10.1002/smll.v14.1110.1002/smll.201703755.

[20] S. Ma, J. Gu, Y. Han, Y. Gao, Y. Zong, Z. Ye, J. Xue, Facile fabrication of C-TiO_2 nanocomposites with enhanced photocatalytic activity for degradation of tetracycline, ACS Omega 4 (25) (2019) 21063–21071, https://doi.org/10.1021/acsomega.9b02411.

[21] W. Wang, F. Lin, B. Yan, Z. Cheng, G. Chen, M. Kuang, C. Yang, L. Hou, The role of seashell wastes in TiO_2/seashell composites: photocatalytic degradation of methylene blue dye under sunlight, Environ. Res. 188 (2020) 109831, https://doi.org/10.1016/j.envres.2020.109831.

[22] U.G. Eziefula, J.C. Ezeh, B.I. Eziefula, Properties of seashell aggregate concrete: a review, Constr. Build. Mater. 192 (2018) 287–300, https://doi.org/10.1016/j.conbuildmat.2018.10.096.

[23] C. XU, T. ETCHEVERRY, Hydro-liquefaction of woody biomass in sub- and super-critical ethanol with iron-based catalysts, Fuel. 87 (3) (2008) 335–345, https://doi.org/10.1016/j.fuel.2007.05.013.

[24] L. Zhang, P. Champagne, C. (Charles),, Xu, Bio-crude production from secondary pulp/paper-mill sludge and waste newspaper via co-liquefaction in hot-compressed water, Energy. 36 (2011) 2142–2150, https://doi.org/10.1016/j.energy.2010.05.029.

[25] Xingzhong Yuan, Jingyu Wang, Guangming Zeng, Huajun Huang, Xiaokai Pei, Hui Li, Zhifeng Liu, Minghui Cong, Comparative studies of thermochemical liquefaction characteristics of microalgae using different organic solvents, Energy. 36 (11) (2011) 6406–6412, https://doi.org/10.1016/j.energy.2011.09.031.

[26] S. Ding, F. Huang, X. Mou, J. Wu, X. Lü, Mesoporous hollow TiO_2 microspheres with enhanced photoluminescence prepared by a smart amino acid template, J. Mater. Chem. 21 (2011) 4888–4892, https://doi.org/10.1039/c0jm03628e.

[27] M. Nevárez-Martínez, M. Kobylański, P. Mazierski, J. Wółkiewicz, G. Trykowski, A. Malankowska, M. Kozak, P. Espinoza-Montero, A. Zaleska-Medynska, Self-organized TiO_2-MnO_2 nanotube arrays for efficient photocatalytic degradation of toluene, Molecules. 22 (2017) 564, https://doi.org/10.3390/molecules22040564.

[28] Shu Wang, Lei Zhao, Lina Bai, Junmin Yan, Qing Jiang, Jianshe Lian, Enhancing photocatalytic activity of disorder-engineered C/TiO_2 and TiO_2 nanoparticles, J. Mater. Chem. A. 2 (20) (2014) 7439–7445, https://doi.org/10.1039/C4TA00354C.

[29] J.L. Figueiredo, Functionalization of porous carbons for catalytic applications, J. Mater. Chem. A. 1 (2013) 9351–9364, https://doi.org/10.1039/c3ta10876g.

[30] Lingli Zhu, Dekui Shen, Kai Hong Luo, A critical review on VOCs adsorption by different porous materials: species, mechanisms and modification methods, J. Hazard. Mater. 389 (2020) 122102, https://doi.org/10.1016/j.jhazmat.2020.122102.

[31] Limin Li, Xuming Zhang, Guosong Wu, Xiang Peng, Kaifu Huo, Paul K. Chu, Supercapacitor electrodes based on hierarchical mesoporous MnOx/Nitrided TiO_2 nanorod arrays on carbon fiber paper, Adv. Mater. Interfaces 2 (6) (2015) 1400446, https://doi.org/10.1002/admi.201400446.

[32] Ming Wu, Xin He, Binghua Jing, Teng Wang, Chengyin Wang, Yanlin Qin, Zhimin Ao, Shaobin Wang, Taicheng An, Novel carbon and defects co-modified g-C_3N_4 for highly efficient photocatalytic degradation of bisphenol a under visible light, J. Hazard. Mater. 384 (2020) 121323, https://doi.org/10.1016/j.jhazmat.2019.121323.

[33] Xin He, Ming Wu, Zhimin Ao, Bo Lai, Yanbo Zhou, Taicheng An, Shaobin Wang, Metal–organic frameworks derived C/TiO_2 for visible light photocatalysis: simple synthesis and contribution of carbon species, J. Hazard. Mater. 403 (2021) 124048, https://doi.org/10.1016/j.jhazmat.2020.124048.

[34] J. Yu, S. Wang, J. Low, W. Xiao, Enhanced photocatalytic performance of direct Z-scheme g-C_3N_4-TiO_2 photocatalysts for the decomposition of formaldehyde in air, Phys. Chem. Chem. Phys. 15 (2013) 16883–16890, https://doi.org/10.1039/c3cp53131g.

[35] Jiejing Zhang, Yajie Hu, Hong Zheng, Pengyi Zhang, Hierarchical Z-scheme 1D/2D architecture with TiO_2 nanowires decorated by MnO_2 nanosheets for efficient adsorption and full spectrum photocatalytic degradation of organic pollutants, Catal Sci Technol. 10 (11) (2020) 3603–3612, https://doi.org/10.1039/D0CY00419G.

[36] Fawei Lin, Zhi Wang, Zhiman Zhang, Li Xiang, Dingkun Yuan, Beibei Yan, Zhihua Wang, Guanyi Chen, Comparative investigation on chlorobenzene oxidation by oxygen and ozone over a MnOx/Al_2O_3 catalyst in the presence of SO_2, Environ. Sci. Technol. 55 (5) (2021) 3341–3351, https://doi.org/10.1021/acs.est.0c0786210.1021/acs.est.0c07862.s001.

[37] Z. Zhang, F. Lin, L. Xiang, H. Yu, Z. Wang, B. Yan, G. Chen, Synergistic effect for simultaneously catalytic ozonation of chlorobenzene and NO over MnCoOx catalysts: byproducts formation under practical conditions, Chem. Eng. J. 427 (2022), 130929, https://doi.org/10.1016/j.cej.2021.130929.

[38] Zhiman Zhang, Li Xiang, Fawei Lin, Zhi Wang, Beibei Yan, Guanyi Chen, Catalytic deep degradation of Cl-VOCs with the assistance of ozone at low temperature over MnO_2 catalysts, Chem. Eng. J. 426 (2021) 130814, https://doi.org/10.1016/j.cej.2021.130814.

[39] Y. Zhang, M. Wu, Y. Wang, Y.H. Kwok, W. Pan, W. Szeto, H. Huang, D.Y.C. Leung, Fluorinated TiO_2 coupling with α-MnO_2 nanowires supported on different substrates for photocatalytic VOC abatement under vacuum ultraviolet irradiation, Appl. Catal. B: Environ. 280 (2020), 119388, https://doi.org/10.1016/j.apcatb.2020.119388.

[40] Seunghyun Weon, Eunji Choi, Hyejin Kim, Jee Yeon Kim, Hee-Jin Park, Sae-mi Kim, Wooyul Kim, Wonyong Choi, Active 001 facet exposed TiO2 nanotubes photocatalyst filter for volatile organic compounds removal: from material development to commercial indoor air cleaner application, Environ. Sci. Technol. 52 (16) (2018) 9330–9340, https://doi.org/10.1021/acs.est.8b0228210.1021/acs.est.8b02282.s001.

[41] H. Chu, W. Lei, X. Liu, J. Li, W. Zheng, G. Zhu, C. Li, L. Pan, C. Sun, Synergetic effect of TiO_2 as co-catalyst for enhanced visible light photocatalytic reduction of Cr(VI) on $MoSe_2$, Appl. Catal. Gen. 521 (2016) 19–25, https://doi.org/10.1016/j.apcata.2016.01.022.

[42] Panjie Li, Wang Cao, Yu Zhu, Qiuyi Teng, Lu Peng, Caiyun Jiang, Changsheng Feng, Yuping Wang, NaOH-induced formation of 3D flower-sphere BiOBr/Bi_4O_5Br 2 with proper-oxygen vacancies via in-situ self-template phase transformation method for antibiotic photodegradation, Sci. Total. Environ. 715 (2020) 136809, https://doi.org/10.1016/j.scitotenv.2020.136809.

[43] Bo Niu, Shanshan E, Yilin Cao, Jiefeng Xiao, Lu Zhan, Zhenming Xu, Xu, Utilizing E-Waste for construction of magnetic and core-shell Z-scheme photocatalysts: an effective approach to E-Waste recycling, Environ. Sci. Technol. 55 (2) (2021) 1279–1289, https://doi.org/10.1021/acs.est.0c07266.

[44] Li Liu, Jun Peng, Gang Wang, Yanqing Ma, Feng Yu, Bin Dai, Xu-Hong Guo, Ching-Ping Wong, Synthesis of mesoporous TiO_2@C@MnO_2 multi-shelled hollow nanospheres with high rate capability and stability for lithium-ion batteries, RSC Adv. 6 (69) (2016) 65243–65251, https://doi.org/10.1039/C6RA14156K.

[45] D.-L. Chen, H. Shang, W. Zhu, R. Krishna, Transient breakthroughs of CO_2/CH_4 and C_3H_6/C_3H_8 mixtures in fixed beds packed with Ni-MOF-74, Chem. Eng. Sci. 117 (2014) 407–415, https://doi.org/10.1016/j.ces.2014.07.008.

[46] Zhao Hu, Chao Yang, Kangle Lv, Xiaofang Li, Qin Li, Jiajie Fan, Single atomic Au induced dramatic promotion of the photocatalytic activity of TiO_2 hollow

microspheres, Chem. Commun. 56 (11) (2020) 1745–1748, https://doi.org/10.1039/C9CC08578E.

[47] Mengmeng Huang, Yingxuan Li, Mengwei Li, Jie Zhao, Yunqing Zhu, Chuanyi Wang, Virender K. Sharma, Active site-directed tandem catalysis on single platinum nanoparticles for efficient and stable oxidation of formaldehyde at room temperature, Environ. Sci. Technol. 53 (7) (2019) 3610–3619, https://doi.org/10.1021/acs.est.9b01176.

[48] Greta M. Haselmann, Bettina Baumgartner, Jia Wang, Karin Wieland, Tushar Gupta, Christopher Herzig, Andreas Limbeck, Bernhard Lendl, Dominik Eder, In situ Pt photodeposition and methanol photooxidation on Pt/TiO_2: pt-loading-dependent photocatalytic reaction pathways studied by liquid-phase infrared spectroscopy, ACS Catal. 10 (5) (2020) 2964–2977, https://doi.org/10.1021/acscatal.9b05588.

[49] Jieyuan Li, Ruimin Chen, Wen Cui, Xing'an Dong, Hong Wang, Ki-Hyun Kim, Yinghao Chu, Jianping Sheng, Yanjuan Sun, Fan Dong, Synergistic photocatalytic decomposition of a volatile organic compound mixture: high efficiency, reaction mechanism, and long-term stability, ACS Catal. 10 (13) (2020) 7230–7239, https://doi.org/10.1021/acscatal.0c00693.

[50] Fang Liu, Xiaopan Liu, Jie Shen, Addie Bahi, Shiying Zhang, Long Wan, Frank Ko, The role of oxygen vacancies on Pt/$NaInO_2$ catalyst in improving formaldehyde oxidation at ambient condition, Chem. Eng. J. 395 (2020) 125131, https://doi.org/10.1016/j.cej.2020.125131.

[51] J. Li, H. Na, X. Zeng, T. Zhu, Z. Liu, In situ DRIFTS investigation for the oxidation of toluene by ozone over Mn/HZSM-5, Ag/HZSM-5 and Mn-Ag/HZSM-5 catalysts, Appl. Surf. Sci. 311 (2014) 690–696, https://doi.org/10.1016/j.apsusc.2014.05.138.

[52] Xueqin Yang, Xiaolin Yu, Meizan Jing, Weiyu Song, Jian Liu, Maofa Ge, Defective $MnxZr_{1-x}O_2$ solid solution for the catalytic oxidation of toluene: insights into the oxygen vacancy contribution, ACS Appl. Mater. Inter. 11 (1) (2019) 730–739, https://doi.org/10.1021/acsami.8b17062.

[53] Junxian Qin, Jun Wang, Junjie Yang, Yun Hu, Mingli Fu, Daiqi Ye, Metal organic framework derivative-TiO_2 composite as efficient and durable photocatalyst for the degradation of toluene, Appl. Catal. B: Environ. 267 (2020) 118667, https://doi.org/10.1016/j.apcatb.2020.118667.